

# Role and Mechanism of a Micro-/Nano-Structured Porous Zirconia Surface in Regulating the Biological Behavior of Bone Marrow Mesenchymal Stem Cells

Yuan Gao, Qian Ding, Wenjin Li, Ranli Gu, Ping Zhang,\* and Lei Zhang\*



Cite This: *ACS Appl. Mater. Interfaces* 2023, 15, 14019–14032



Read Online

ACCESS |

Metrics & More

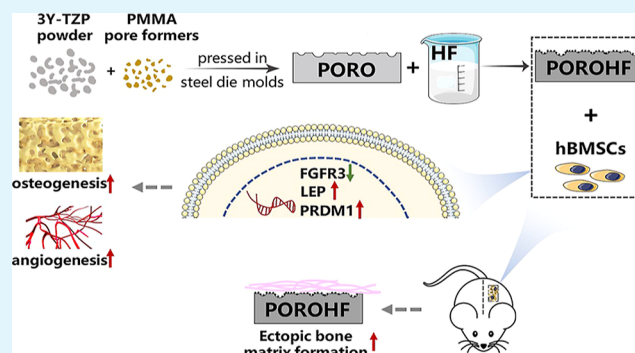
Article Recommendations

Supporting Information

**ABSTRACT:** Zirconia as a promising dental implant material has attracted much attention in recent years. Improving the bone binding ability of zirconia is critical for clinical applications. Here, we established a distinct micro-/nano-structured porous zirconia through dry-pressing with addition of pore-forming agents followed by hydrofluoric acid etching (POROHF). Porous zirconia without hydrofluoric acid treatment (PORO), sandblasting plus acid-etching zirconia, and sintering zirconia surface were applied as controls. After human bone marrow mesenchymal stem cells (hBMSCs) were seeded on these four groups of zirconia specimens, we observed the highest cell affinity and extension on POROHF. In addition, the POROHF surface displayed an improved osteogenic phenotype in contrast to the other groups.

Moreover, the POROHF surface facilitated angiogenesis of hBMSCs, as confirmed by optimal stimulation of vascular endothelial growth factor B and angiopoietin 1 (ANGPT1) expression. Most importantly, the POROHF group demonstrated the most obvious bone matrix development in vivo. To investigate further the underlying mechanism, RNA sequencing was employed and critical target genes modulated by POROHF were identified. Taken together, this study established an innovative micro-/nano-structured porous zirconia surface that significantly promoted osteogenesis and investigated the potential underlying mechanism. Our present work will improve the osseointegration of zirconia implants and help further clinical applications.

**KEYWORDS:** dental implant, micro-/nano-structured porous zirconia, hBMSCs, osteogenesis, angiogenesis, RNA sequencing



## INTRODUCTION

Zirconia material, especially 3 mol % yttrium oxide stabilized polycrystalline tetragonal phase zirconia (3Y-TZP), has become widely used in dentistry in recent years. Y-TZP shows good biocompatibility, high chemical resistance and fracture toughness, reliable flexural strength, and decreased bacterial intraoral biofilm formation compared with titanium.<sup>1,2</sup> In addition, it is aesthetically pleasing, especially fit in the anterior teeth area.<sup>1,2</sup> With continuous development of the properties of zirconia material and the digital processing technique, zirconia has become a suitable choice for dental implant materials. Despite this, a systematic review<sup>3</sup> reported an overall failure rate of 7.21% for the included 1704 zirconia implants; 83.7% of the failures were due to a lack or loss of osseointegration. Another systematic review of preclinical studies<sup>4</sup> revealed significantly decreased removal torque values and slower initial osseointegration for roughened surface zirconia compared to titanium. Therefore, improving the bone-bonding ability of zirconia will aid in its clinical use.

Surface microtopography has been demonstrated to predominantly influence implant osseointegration. Recent studies have explored ways to modify zirconia implant surfaces

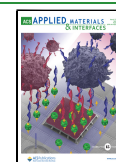
for better osseointegration, including acid etching,<sup>5</sup> sandblasting,<sup>6</sup> laser treatment,<sup>7</sup> ultraviolet light,<sup>8</sup> and coatings.<sup>1,9–11</sup> Although sandblasting and acid etching is the most common zirconia surface treatment,<sup>12,13</sup> it is difficult to obtain a multiscale gradient porous surface similar to the well-established sandblasted, large-grit, acid-etched surfaces of titanium implants. Additionally, compared to bone tissue, zirconia has a much higher elastic modulus. A stress shielding effect around the dental implant-bone interface can lead to detrimental resorptive bone remodeling and even loss of osseointegration.<sup>14,15</sup>

The above issues led to the concept of functional graded zirconia with a porous surface, which can be obtained by sol-gel chemistry,<sup>16</sup> coating,<sup>17</sup> three-dimensional (3D) printing,<sup>18</sup>

**Received:** December 18, 2022

**Accepted:** February 27, 2023

**Published:** March 13, 2023



or dry-pressing with addition of pore-forming agents.<sup>19</sup> In a previous study, 3D printed porous zirconia scaffolds with Zn-HA/glass composite coating exhibited superior cell adhesion, distribution, and osteogenic differentiation ability.<sup>18</sup> We previously generated zirconia with a porous surface structure, with an average pore size of 300  $\mu\text{m}$ .<sup>20</sup> However, it exhibited an inhibitory effect on osteogenesis, presumably because the pore size was too large and, more critically, the porous surface lacked a micro–nano structure. Recent research has revealed that combined nano- and micro-scale topographies can significantly modulate the cell response and promote adhesion, proliferation, and differentiation.<sup>7</sup> Therefore, we hypothesize that combining a pore-forming technique and acid etching to produce a multi-scale zirconia surface structure will improve the bone-bonding ability of zirconia.

The previous study of the interaction between the micro-/nano-structured zirconia surface and stem cells is rare, and the specific mechanism of action is unclear. The aim of this study was to construct a zirconia surface with micro-scale pores combining nano-scale rough structures, investigate its effects on osteogenesis and angiogenesis, and explore the underlying mechanism. The results demonstrated that micro-/nano-structured porous zirconia had good biocompatibility, facilitated angiogenesis, and promoted osteogenesis *in vitro* and *in vivo*. Mechanistically, the critical target genes *FGFR3*, *LEPTIN* (*LEP*), and *PRDM1* were identified. Overall, we provide valuable clues for the potential use of micro-/nano-structured porous surface as an effective modification for zirconia implants.

## MATERIALS AND METHODS

**Specimens.** Zirconia specimens were divided into four groups according to different surface treatments as follows:

**Control Group.** No surface treatment after sintering.

**Sandblasting and Hydrofluoric Acid Etching Group.** Sandblasted with 110  $\mu\text{m}$   $\text{Al}_2\text{O}_3$  particles at 0.45 MPa (Ovaljet HiBlaster, SHOFU) and then etched in 40% hydrofluoric acid solution at room temperature (RT) for 60 min.<sup>1,5,13</sup>

**Porous Group.** The starting material was 3Y-TZP powder (400 nm,  $\text{ZrO}_2$  94.5 wt %;  $\text{Y}_2\text{O}_3$  5.15 wt %; impurities  $\text{SiO}_2 + \text{Fe}_2\text{O}_3 + \text{Na}_2\text{O} \leq 0.07$  wt %, Zhong Xin Tang Guo Ye Medical Technology Co., Ltd., China). The mixtures of raw materials were wet-milled at a rotating rate of 300 rpm in a planetary ball mill for 3 h using absolute ethyl alcohol as the dispersant. The mixtures were pressed in steel die molds to obtain disc-like green bodies. Polymethyl methacrylate pore formers with an average diameter of 200  $\mu\text{m}$  were added to the mixtures at 3% (w/w) and removed from the green body by burning in an air furnace at 300  $^\circ\text{C}$  for 3 h to create the expected porous structures. The porous zirconia specimens were obtained after sintering in ambient atmosphere at 1520  $^\circ\text{C}$  with an isothermal exposure time of 2 h and then cooling down to RT naturally.<sup>20</sup>

**Porous Plus Hydrofluoric Acid Group.** To increase the surface nanostructure, secondary surface treatment of porous zirconia specimens was carried out by acid etching with 40% hydrofluoric acid, followed by cleaning the surface with running water and high-pressure air and ultrasonically cleaning with deionized water ( $\text{dH}_2\text{O}$ ) three times for 20 min each.

All specimens were immersed in acetone, absolute alcohol, and  $\text{dH}_2\text{O}$  (Milli-Q Ultra-Pure, Millipore, Billerica, MA, USA) sequentially and washed in an ultrasonic cleaner for 20 min each and then sterilized in an autoclave at 120  $^\circ\text{C}$  for 30 min before *in vitro* and *in vivo* experiments after drying for 24 h.

**Surface Characterization.** Field emission scanning electron microscopy (FESEM; S4800, Hitachi, Japan) was used to observe surface morphology. The surface element distribution was examined using FESEM with its own energy dispersive spectrometer (EDS).

The average pore size and porosity of the porous materials were examined by mercury intrusion porosimetry using a high-performance fully automated mercury-pressure instrument (AutoPore IV 9500, Micromeritics, Norcross, GA, USA). The surface roughness of the control group (CTRL) and sandblasting and hydrofluoric acid etching (SBHF) groups and the flat area between the pores of the two porous groups were measured by a 3D laser microscope (VK-X200, Keyence, Japan). Ten 50  $\times$  50  $\mu\text{m}$  surface areas with no obvious processing defects were selected for laser scanning and analysis. The static contact angle of water was measured by a contact angle meter (OCA50, Dataphysics, Germany).

**X-ray Diffraction Measurements.** X-ray diffraction (XRD) analysis was conducted on an X-ray diffractometer (D/max 2500, Rigaku, Japan) with a  $\text{Cu K}\alpha$  source over a diffraction angle ( $2\theta$ ) ranging from 25–35 $^\circ$ , with a step interval of 1 s and step size of 0.02 $^\circ$ . The monoclinic peak intensity ratio and monoclinic phase content were calculated according to formulas in literature.<sup>21,22</sup>

**Flexural Strength Measurements.** Zirconia bars (20 mm  $\times$  4 mm  $\times$  1.4 mm) with the porous surface and solid base were fabricated. A three-point bending test with 15 specimens for each group was performed following the ISO 6872:2015 standard. Loading was performed using a universal testing machine (AGS-X, SHIMADZU, Kyoto, Japan) with a crosshead speed of 1 millimeter per minute and a loading span of 16 mm until failure occurred.

**hBMSC Culture and Osteogenic Induction.** hBMSCs from three healthy adult donors were obtained from ScienCell Company (San Diego, CA, USA). Cells were cultured in  $\alpha$ -minimum essential medium ( $\alpha$ -MEM; Gibco, Grand Island, NY, USA) supplemented with 10% (v/v) fetal bovine serum (FBS) and 1% (v/v) penicillin/streptomycin (Pen/Strep) (all from Gibco, Thermo Fisher Scientific, Waltham, MA, USA) at 37  $^\circ\text{C}$  in an incubator with 95% air and 5%  $\text{CO}_2$  and 100% relative humidity. Cells were subcultured at 90% confluency. P3–P4 hBMSCs were used in subsequent tests. All *in vitro* experiments were repeated three times unless otherwise stated.  $\alpha$ -MEM with 10% (v/v) FBS and 1% (v/v) Pen/Strep was employed as the proliferation medium (PM).  $\alpha$ -MEM with 10% (v/v) FBS, 1% (v/v) Pen/Strep, 10 nM dexamethasone, 10 mM  $\beta$ -glycerophosphate, and 50 mg/mL L-ascorbic acid was employed as the osteogenic medium (OM).

**Biocompatibility Assessment In Vitro. Cell Morphology and Adhesion.** The four groups of zirconia specimens ( $\Phi 10 \times 1.5$  mm) were placed in 48-well plates, and hBMSCs were incubated on the material surface at a density of 7000 cells/well for 4 h, 24 h, and 7 days. The original medium was discarded, and cells from each timepoint were fixed with 4% paraformaldehyde for 30 min followed by three gentle washes with phosphate-buffered saline (PBS), gradient ethanol dehydration, drying in a critical point desiccator (Micro Modul YO-230, Thermo Fisher Scientific), and observed under FESEM after surface sputtering with gold plating.

Cell adhesion was observed by laser scanning confocal microscopy (LSCM; LSM 710; Zeiss). Briefly, hBMSCs were incubated on each of the four groups of zirconia ( $\Phi 10 \times 1.5$  mm) for 24 h and rinsed three times with PBS. Cells were then fixed with 4% paraformaldehyde for 30 min at RT, followed by 7 min of permeabilization with 0.1% Triton X-100 in PBS. After washing with PBS, cells were stained with 5 g/mL FITC-conjugated phalloidin for 40 min and DAPI (Sigma, St. Louis, MO, USA) for 5 min before visualization by LSCM at wavelengths of 488 nm (green, FITC-labeled phalloidin) and 405 nm (blue, DAPI).

**Live/Dead Cell Staining.** Zirconia specimens ( $\Phi 10 \times 1.5$  mm) were placed in 48-well plates, and hBMSCs were cultured at a density of 8000 cells/well on the surface. Afterward, cells were washed three times with PBS and incubated for 30 min at RT with 2  $\mu\text{M}$  calcein-AM and 8  $\mu\text{M}$  propidium iodide (Live/Dead Viability/Cytotoxicity Assay for Animal Cells; KeyGen Biotech Corp., Ltd., Nanjing, China). A fluorescent microscope (BX43, Olympus, Japan) was used to observe the cells after three washes with PBS.

**Cell Proliferation.** hBMSCs were incubated in 48-well plates at a density of  $1.5 \times 10^4$  cells/well on zirconia specimens. Cell Counting Kit-8 (CCK8; Dojindo Laboratories, Kumamoto, Japan) was used to

measure the number of cells adhering to sample surfaces after incubation for 1, 3, and 5 days. At each time point, the medium was replaced with the counting reagent and cells were incubated for 2 h according to the manufacturer's instructions. A microplate reader (ELx808; Biotek, Winooski, VT, USA) was used to measure spectrophotometric absorbance at 450 nm for each well. Each group was tested in triplicate.

**Protein Adsorption Assay.** After adding 100 mg/mL FITC-labeled bovine serum albumin (BSA) to the surface, specimens were incubated at 37 °C for 1 h. Three washes with PBS were performed to remove unabsorbed protein before scanning at 488 nm using a fluorescent microscope (BX43, Olympus, Japan).

**Osteogenic and Angiogenic Effects In Vitro.** hBMSCs were seeded in 24-well plates on specimens ( $\Phi 15 \times 1.5$  mm) at a density of  $5 \times 10^4$  cells/well and divided into six groups: CTRL, SBHF, porous group (PORO), porous plus hydrofluoric acid group (POROHF), OM, and PM. At 70–80% confluency, OM was added to all groups except PM. The medium was changed every 2 days and osteogenic and angiogenic effects were evaluated.

**Alkaline Phosphatase Staining and Quantification.** Alkaline phosphatase (ALP) staining was performed according to the manufacturer's instructions using the ALP staining kit (Biyuntian, Shanghai, China) after culturing for 7 or 14 days. ALP activity was quantified at the same time. An ALP activity kit (Jiancheng Co., China) was used according to the manufacturer's instructions. Cells were lysed with 1% Triton X-100. A bicinchoninic acid (BCA) protein assay kit (Pierce Thermo Scientific, Waltham, MA, USA) was used to determine total protein content. Protein samples were then incubated with the substrate solution for 15 min at 37 °C, and the color development reagent was added to each well. Absorbance was measured at 520 nm, and ALP activity was calculated.

**Alizarin Red S Staining and Quantification.** hBMSCs were fixed in 4% paraformaldehyde for 30 min at RT on days 14 and 21 of osteogenic induction. Cells were then rinsed three times with distilled water before treatment with alizarin red S (ARS) solution (2%, pH 4.2, Sigma-Aldrich). To quantify matrix calcification, 10% (w/v) cetylpyridinium chloride (Sigma-Aldrich) was added to dissolve the ARS stain. The solution was collected, and the absorbance was detected at 562 nm.

**RNA Extraction and Real-Time Quantitative PCR.** Total cellular RNA was extracted on day 14 after osteoinduction using the TRIzol reagent (Invitrogen, Carlsbad, CA, USA) and reverse-transcribed to first strand cDNA using the Prime Script RT Reagent Kit (Takara, Tokyo, Japan) according to the manufacturer's instructions. Real-time quantitative PCR (RT-qPCR) was performed using an ABI Prism 7500 Real-Time PCR System (Applied Biosystems, Foster City, CA, USA) and Power SYBR Green PCR Master Mix (Roche Applied Science, Mannheim, Germany). Primer sequences for human *GAPDH*, *RUNX2*, *ALP*, *VEGFB*, *ANGPT1* (*ANG-1*), *FGFR3*, *PRDMI*, and *LEP* are listed in Table 1.

**In Vivo Ectopic Osteogenesis.** This study was approved by the Experimental Animal Welfare Ethics Subcommittee of the Biomedical Ethics Committee of Peking University (LA2021524). P3 hBMSCs were seeded at a density of  $5 \times 10^4$  cells/mL on the surfaces of  $6 \times 5 \times 1$  mm rectangular zirconia specimens in the following groups: CTRL, SBHF, PORO, and POROHF. At 70–80% confluency, OM was added to all the groups, and 7 days after osteogenesis induction, 8 week-old male BALB/c homozygous nude (nu/nu) mice were anesthetized with 1% (mass fraction) sodium pentobarbital, and an incision of approximately 10 mm was made in the midline of the dorsal skin. After blunt separation using hemostatic forceps, the cell–material complex was carefully implanted (Figure S3A). The implants and their surrounding tissues were harvested at 8 weeks following surgery; each group included 10 specimens. The tissues were formalin-fixed and resin-infiltrated, and hard tissue slices were examined under a light microscope (BX43, Olympus, Japan) following hematoxylin and eosin (HE) and toluidine blue staining.

**RNA Sequencing.** hBMSCs were seeded at a density of  $5 \times 10^4$  cells/mL on specimens ( $\Phi 15 \times 1.5$  mm). Total cellular RNA was extracted on day 14 after induction. Raw reads with low quality were

**Table 1. Primer Sequences for RT-qPCR**

gene	primer	5'–3' sequence
<i>GAPDH</i>	forward	GCCCCCTCTGCTGATGCC
	reverse	GGGTGGCAGTGTGGCATGGA
<i>RUNX2</i>	forward	CCGCCATGCACCACCACCT
	reverse	CTGGGCCACTGCTGAGGAATTT
<i>ALP</i>	forward	ATGGGATGGGTGTCTCCACA
	reverse	CCACGAAGGGGAAGCTTGTC
<i>VEGFB</i>	forward	GCTTAGAGCTCAACCCAGACACC
	reverse	CAAGTCACCCCTGCTGAGTCTGAA
<i>ANGPT1</i>	forward	TCGTGAGACTACGATGCCA
	reverse	TCTCCGAGTTCATGTTTCCAC
<i>FGFR3</i>	forward	TGGCGTGGGAGACAAGTTT
	reverse	GCACGGTAACGTAGGGTGTG
<i>PRDMI</i>	forward	TAAAGCAACCGAGCACTGAGA
	reverse	ACGGTAGAGTCTTCTTCTTTG
<i>LEP</i>	forward	TGCCTTCCAGAAACGTGATCC
	reverse	CTCTGTGGAGTAGCCTGAAGC

discarded, and adaptors were removed. Reads were mapped to the human genome (GRCh38) using Tophat2 software<sup>23</sup> (<http://ccb.jhu.edu/software/tophat>), and FPKM (fragments per kilobase of exon model per million mapped fragments) were calculated with Cufflinks software<sup>24</sup> (<http://cufflinks.cbc.umd.edu/>). Cuffdiff, part of the Cufflinks package, was used to identify differentially expressed genes (DEGs). Genes with FPKM < 0.1 in both the control and experimental group were ignored in the subsequent analysis. Gene ontology (GO) and gene set enrichment analysis (GSEA) were performed by R package cluster Profiler. R package ggplot2 and pheatmap were used to draw pictures. RT-qPCR was performed to confirm the expression levels of representative DEGs.

**Statistical Analysis.** All experiments were performed in triplicate unless otherwise stated. All results are presented as the mean  $\pm$  standard deviation. Student's *t*-tests were conducted to compare differences between two groups; comparisons between more than two groups were analyzed by one-way ANOVA followed by a Tukey's post-hoc test using SPSS 21.0 software (SPSS Inc., Chicago, IL, USA). *p* < 0.05 indicated statistical significance (\**p* < 0.05; \*\**p* < 0.01; \*\*\**p* < 0.001).

## RESULTS AND DISCUSSION

**Surface Characterization of the Micro-/Nano-structured Porous Zirconia.** In this study, a porous zirconia surface with nanostructure was successfully fabricated by dry-pressing with pore formers and acid etching with hydrofluoric acid. As shown in Figure 1A, pore structures were evenly distributed on surfaces of the PORO and POROHF groups. The average pore diameter was 211.75  $\mu$ m (Figure 1B), and the porosity was 24.40%. The POROHF group presented nanometric granular textures sized 50–500 nm inside the pores (Figure 1A). Hydrofluoric acid etching significantly increased the surface roughness inside and between the pores in the POROHF group (Figure 1E,G). Ding et al.<sup>13</sup> revealed that zirconia implants with micro- and nano-roughened surfaces demonstrated better osseointegration than sintered implants. The hydrophilicity of the POROHF group was also improved significantly ( $12.78 \pm 2.2^\circ$ , hyper-hydrophilic) (Figure 1F,H). Biologically, materials with lower contact angles are more hydrophilic, which means they are more desirable for protein adsorption, osteoblast proliferation, and osseointegration.<sup>25</sup> Surface characteristics, roughness, and hydrophilicity of the CTRL and SBHF groups were consistent with previous studies.<sup>26,27</sup>

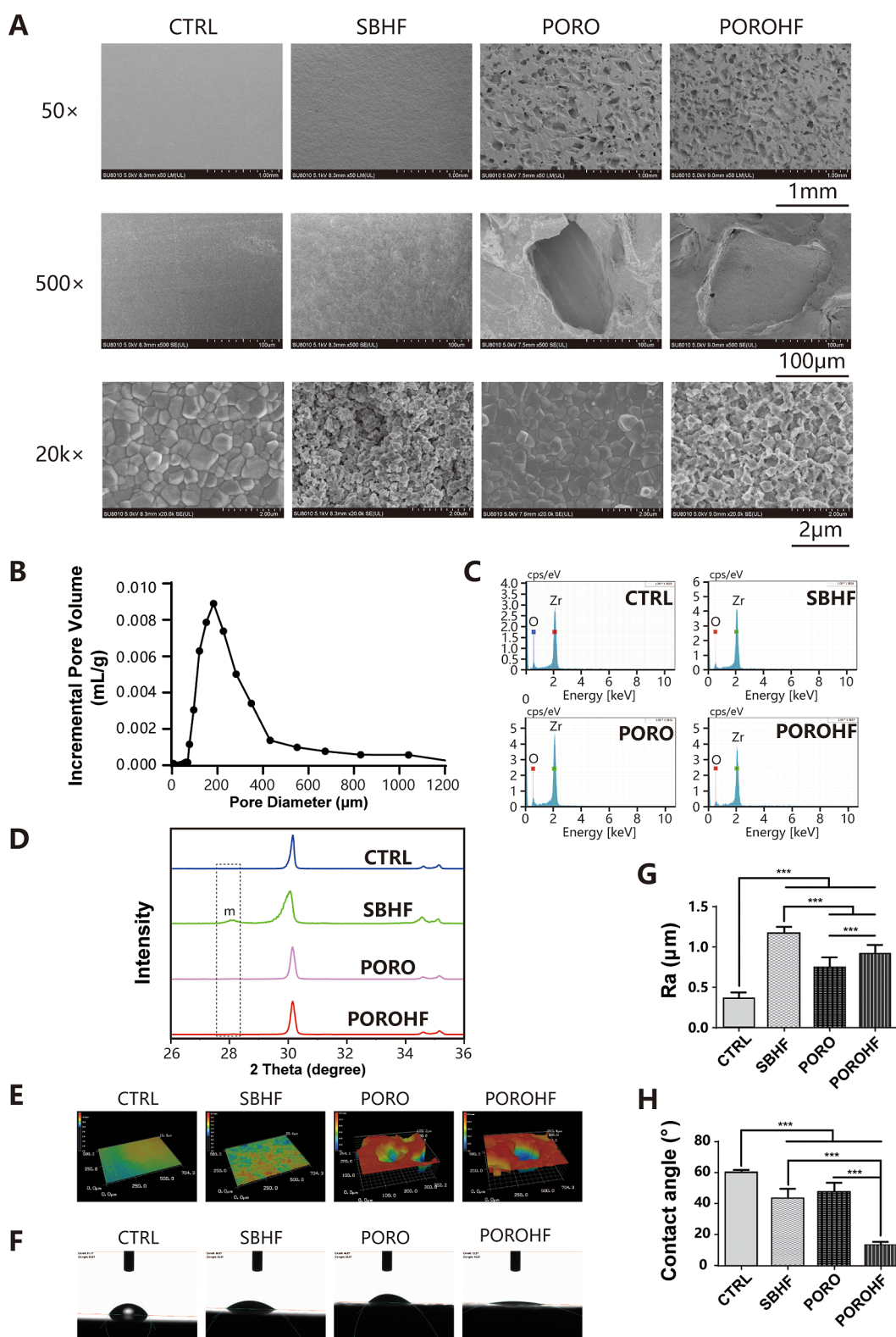


**Figure 1.** Surface characterization of zirconia specimens from four groups. (A) FESEM observation (top view) at 50×, 500×, and 20,000× magnification. (B) MIP detection of pore size distribution. (C) EDS analysis of surface composition of element. (D) XRD spectra showing a monoclinic-phase peak (m). (E,G) 3D laser microscope investigation of surface morphology and roughness. (F,H) Contact angle meter evaluation of hydrophilicity. Data are presented as mean ± SD.  $n = 9$ . \* $p < 0.05$ , \*\* $p < 0.01$ , \*\*\* $p < 0.001$ .

Several techniques were used to process porous ceramics. Porous zirconia layers have been generated on dense substrates by slip casting using coarse treated particles of 40, 70, and 100 μm.<sup>17</sup> Besides, porous zirconia scaffolds with dimensions of

300–450 μm have been fabricated by 3D printing.<sup>18</sup> However, these porous surfaces lack nano-scale structures. Various micro–nano-structures on titanium implant surfaces by femtosecond laser,<sup>28</sup> plasma spraying,<sup>29</sup> and micro-milling

with chemical treatment have previously been constructed.<sup>30</sup> However, for zirconia implants, methods are relatively limited. Rezaei et al.<sup>31</sup> created hierarchical roughened morphology with meso-scale (50  $\mu\text{m}$ ) grooves, micro-scale (1–10  $\mu\text{m}$ ) valleys, and nano-scale (10–400 nm) nodules on Y-TZP with a femtosecond laser. The nano-scale nodules fabricated by laser had a similar size to the nanometric granular textures in our study. Most laser-treated material surfaces show groove-like structures. Our study is the first to combine pore-forming techniques with acid etching to obtain porous zirconia with micro-/nano-structures. Only Zr and O peaks were detected by EDS on this distinct zirconia, indicating there was no impurity contamination (Figure 1C).

**Phase Composition.** The XRD results (Figure 1D) exhibited no obvious monoclinic phase peak in the CTRL group, and the content of the monoclinic phase was 1.07%. An obvious monoclinic phase peak was detected in the SBHF group, with the monoclinic phase content increasing to 15.80%. This trend was similar to those reported in the literature.<sup>32</sup> The XRD patterns exhibited no obvious monoclinic phase peak for PORO and POROHF groups, and the calculated surface monoclinic phase content was 2.61 and 3.04%, respectively. Hadjicharalambous et al. fabricated a porous zirconia with a total porosity of 50% using pore former particles, and XRD patterns showed a one-phase, highly crystalline tetragonal  $\text{ZrO}_2$ ,<sup>33</sup> which was similar to our results.

**Flexural Strength.** The results are presented in Table 2. The difference in the flexural strength was not significant

**Table 2. Flexural Strength of Porous and Micro-/Nano-Structured Porous Specimens<sup>a</sup>**

group	flexural strength (MPa) ( $\sigma_c$ ) (mean $\pm$ SD)
CTRL	1271.90 $\pm$ 261.74
SBHF	1251.52 $\pm$ 182.60
PORO	1271.42 $\pm$ 143.92
POROHF	1251.49 $\pm$ 158.85

<sup>a</sup>CTRL: control group; SBHF: sandblasting and hydrofluoric acid etching group; PORO: porous group; POROHF: porous plus hydrofluoric acid group.

between CTRL and SBHF ( $p = 0.950$ ) and PORO and POROHF ( $p = 0.652$ ). As specimens with porous surface and solid base, PORO and POROHF exhibited high flexural strength that was statistically similar to CTRL and SBHF groups ( $p > 0.05$ ).

Studies have shown that any inherent defect created during the manufacturing process of the material can be considered as detrimental defects, which can act as stress concentrators during crack nucleation, then the cracks propagated, finally triggering catastrophic failure.<sup>34,35</sup> The porous surface structure can be regarded as a macroscopic surface defect in materials, which may impact the mechanical strength of zirconia.<sup>36</sup> Thus, we fabricated and tested zirconia specimens with the micro-/nano-structured porous surface and solid base. The results showed that the flexural strengths of PORO and POROHF groups were significantly similar to those of CTRL and SBHF groups. Therefore, flexural strength of the zirconia material with porous surface and dense base can meet the clinical requirements. When applied to implants, the micro-/nano-structured porous surface in this study will be designed to minimize its impact on the strength of implant. Based on the previous study<sup>15</sup> and our results, the zirconia implant should

be designed with a porous surface and dense core, and the porous structure should be located from at least 3 mm below the implant platform to reduce the stress concentration around the implant neck.<sup>37</sup> Further, the zirconia implant with the micro-/nano-structured porous surface and a dense core will be fabricated, and the fracture and fatigue strength of the implant will be detected.

**Micro-/Nano-structured Porous Zirconia Promoted hBMSC Adhesion and Proliferation.** FESEM (Figure 2A) revealed that after only 4 h, cells formed obvious filopodia on POROHF surfaces (Figure 2A, first line, red arrow), which became more and longer after 24 h (Figure 2A, second line, red arrow), while flat lamellipodia (Figure 2A, blue arrow) formed in the PORO group. After 7 days of culture, all surfaces were covered by numerous cells (Figure S1). In the POROHF group, cells with polygonal shape and multiple long filopodia attached to the pores. On the PORO surface, cells were spindle-shaped with fewer cells inside the pores. On the SBHF surface, short pseudopodia were observed, while cells on the CTRL surface remained flattened with no pseudopodia (Figure 2A). LSCM images were consistent with FESEM images, in which the POROHF group exhibited polygonal cells in contact with the pores and stretched filamentous pseudopods (Figure 2E). The nanoscale features inside pores had a similar size to filopodia, the actin-driven membrane protrusions (tips of 50–100 nm in diameter) that cells use to probe surfaces.<sup>7</sup> As a result, micro-/nano-structured porous surfaces can alter cellular morphology and attachment and lead to cytoskeletal rearrangement.

The FITC-BSA adsorption assay demonstrated that the POROHF surface exhibited the largest population of protein aggregates, followed by the PORO surface. A small amount of BSA bonded to the conspicuous portion of the SBHF surface, while fluorescence was scarcely visible in the CTRL group (Figure 2B). The biological process after implantation begins with protein adsorption. The proteins bind to receptors on the cell membrane, leading to adhesion, spreading, and proliferation.<sup>7,38–40</sup> The increased surface area and high hydrophilicity contribute to protein adsorption;<sup>41</sup> the POROHF surface resulted in greater protein adsorption, which may lead to faster cell adhesion. Additionally, dense proteins can extend pseudopodia to a larger area, promoting cell extension.

Cell viability was also quantitatively determined by CCK8 assay. On days 1 and 3, cell viability appeared comparable on the four materials. After 5 days of culture, there were more adherent hBMSCs in the two porous groups, compared with SBHF ( $p < 0.05$ ) and CTRL ( $p < 0.001$ ) (Figure 2C), demonstrating that porous structures expand the surface area available for cell adhesion and exhibit perfusion ability to support proliferation into the pores.<sup>42</sup> Live/dead analysis revealed only a few dead hBMSCs on all surfaces (Figure 2D). Overall, the above data demonstrated that micro-/nano-structured porous zirconia exhibited good biocompatibility and promoted hBMSC adhesion and proliferation compared to other groups.

**Micro-/Nano-structured Porous Zirconia Promoted hBMSC Osteogenic Differentiation and Angiogenesis.** To investigate further the osteogenic differentiation potential of hBMSCs on different zirconia surfaces, ALP activity analysis was first performed. As shown in Figure 3A,B, after 14 days of osteogenic induction, the POROHF group demonstrated the greatest osteogenic differentiation, as determined by ALP staining and quantification. ALP activity at 7 days of osteogenic

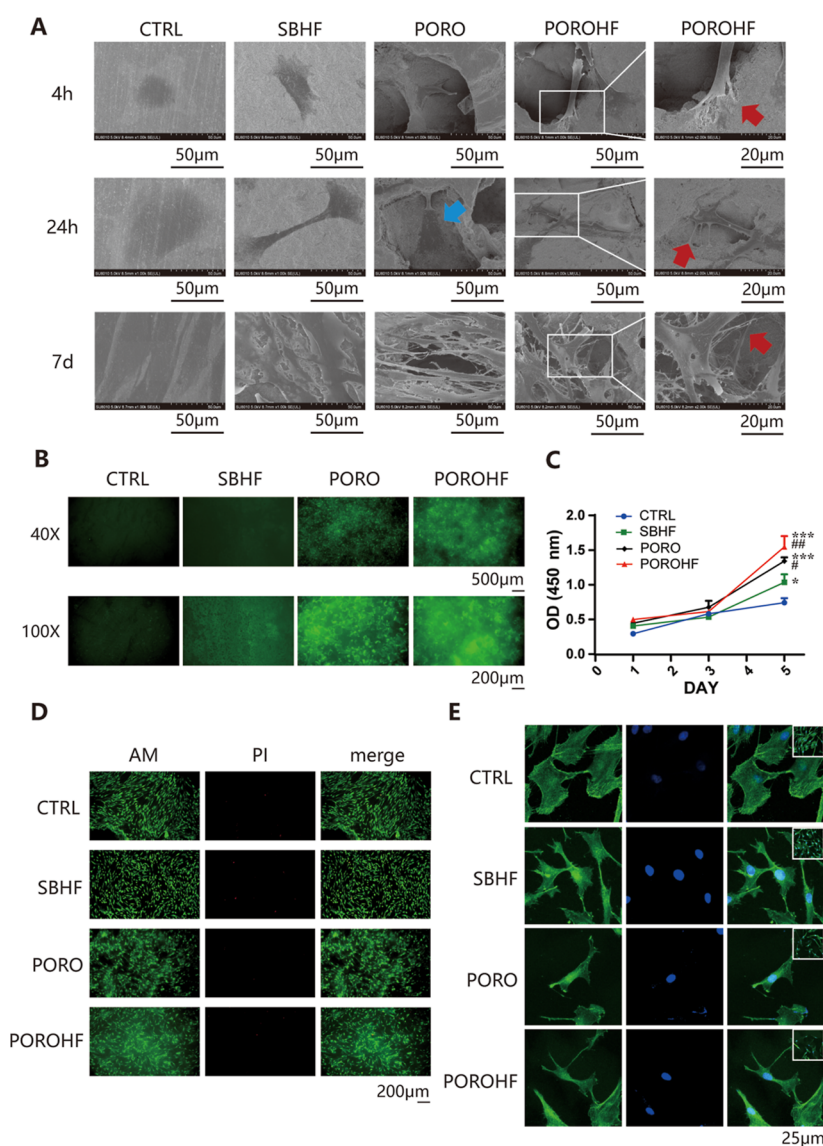


**Figure 2.** Adhesion and proliferation of hBMSCs on POROHF, PORO, SBHF, and CTRL zirconia specimens. (A) FESEM observation of hBMSCs morphology on 4 different surfaces after 4 h, 24 h, and 7 d of culture at 1000 $\times$  magnification. Pseudopodia extending on the POROHF surface were observed at 2000 $\times$  magnification. (B) FITC-BSA adsorption on 4 different surfaces after 1 h incubation at 40 $\times$  and 100 $\times$  magnification. (C) CCK8 assay of adhering hBMSCs on 4 different surfaces after 1, 3, and 5 d of culture. (D) Live/dead cell staining at 100 $\times$  magnification. The green represents live cells, while the red represents dead cells. (E) LSCM micrographs of cellular morphology on 4 different surfaces. Cytoskeleton is stained green and nuclei are stained blue. Data are presented as mean  $\pm$  SD.  $n = 5$ . \*, \*\*, \*\*\* indicate significant differences compared to the CTRL. \* $p < 0.05$ , \*\* $p < 0.01$ , \*\*\* $p < 0.001$ . #, ##, ### indicate significant differences compared to the SBHF. # $p < 0.05$ , ## $p < 0.01$ , ### $p < 0.001$ .

induction showed a consistent trend (Figures 3E and S2D). The POROHF group also showed the highest extracellular matrix mineralization as determined by ARS staining and quantification at 2 weeks after osteogenic induction (Figures S2E and 3F). Microscopy (40 $\times$  and 100 $\times$ ) showed numerous calcium deposit nodules on the surfaces of the PORO and POROHF groups, with the latter showing more nodules and deeper staining (Figure S2E). Additionally, more distinct trends were presented after 21 days of induction ( $p < 0.001$ ) (Figure 3C,D).

Relative mRNA expression of *RUNX2* and *ALP* was also detected to evaluate the effect of different surface morphologies on the osteogenic differentiation of hBMSCs. After 14 days of induction, the POROHF group resulted in the best stimulation of *RUNX2* and *ALP* mRNA expression among all

groups ( $p < 0.001$ ). The PORO group showed greater *RUNX2* and *ALP* expression than the CTRL and SBHF ( $p < 0.001$ ) (Figure 3G), but its *ALP* expression was slightly lower than the POROHF group, with no significant difference between them (Figure 3H). Angiogenic factors were also detected by qPCR. The POROHF group showed the highest *VEGFB* expression ( $p < 0.001$ ). The PORO group also promoted the *VEGFB* expression compared with the CTRL ( $p < 0.001$ ) and SBHF ( $p < 0.05$ ) (Figure 3I). The POROHF and PORO groups exhibited a significantly higher *ANG-1* expression compared to SBHF and CTRL ( $p < 0.001$ ) (Figure 3J). These data strongly indicated the excellent osteoconductive properties of micro-/nano-structured porous zirconia.

Pores are beneficial for bone tissue formation as they allow cell migration and proliferation.<sup>43</sup> Moreover, porous surface

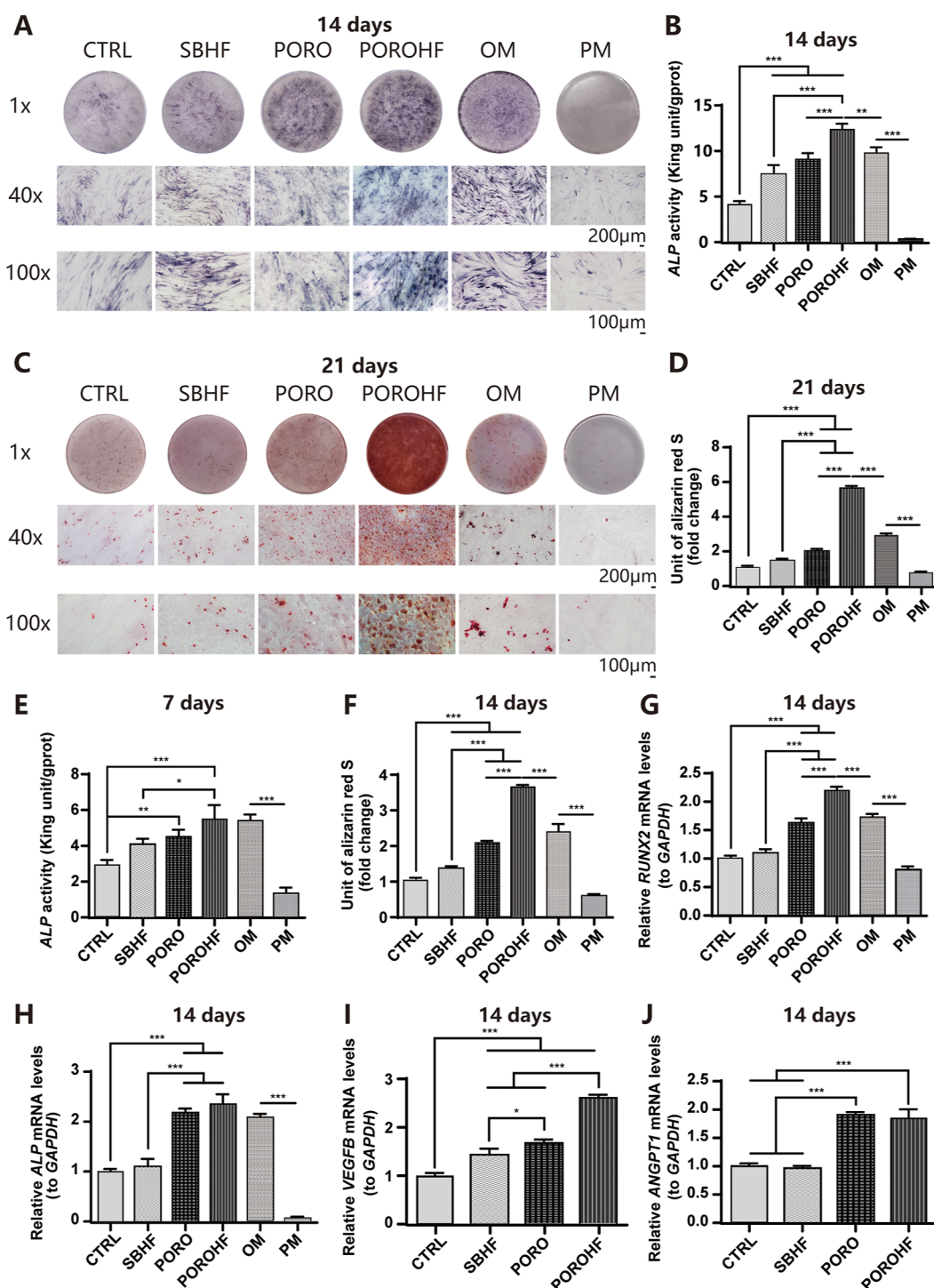


**Figure 3.** Osteogenic and angiogenic differentiation of hBMSCs in CTRL, SBHF, PORO, POROHF, OM, and PM groups in vitro. (A,B) ALP staining and activity of hBMSCs cultured in 6 different groups after 14 days of osteogenic induction. (C,D) Alizarin Red staining and mineralization assay of hBMSCs cultured in 6 different groups after 21 days of osteogenic induction. (E) ALP activity of hBMSCs cultured in 6 different groups after 7 days of osteogenic induction. (F) Mineralization assay of hBMSCs cultured in 6 different groups after 14 days of osteogenic induction. (G,H) Expression of *RUNX2* and *ALP* in hBMSCs cultured in 6 different groups after 14 days of osteogenic induction. (I,J) Expression of *VEGFB* and *ANGPT1* in hBMSCs cultured in POROHF, PORO, SBHF, and CTRL groups after 14 days. Data are presented as mean  $\pm$  SD.  $n = 3$ . \* $p < 0.05$ , \*\* $p < 0.01$ , \*\*\* $p < 0.001$ .

implants can reduce bone resorption induced by stress shielding.<sup>14,15</sup> According to the literature, porous titanium surfaces with diameters of 100–400  $\mu\text{m}$  can facilitate early cell migration and blood vessel formation, as well as osteoblast adhesion, proliferation, and differentiation.<sup>42,44,45</sup> As for pore morphology, cylindrical or spherical porous structures showed

better osteogenic properties.<sup>46,47</sup> Previous studies regarding porous zirconia focused on scaffolds<sup>16,18</sup> and coatings.<sup>17</sup> However, scaffolds are mainly used for bone regeneration, while coatings can undergo delamination and fracture.<sup>1</sup> Hadjicharalambos et al.<sup>35</sup> constructed porous zirconia specimens using pore forming agents and investigated their

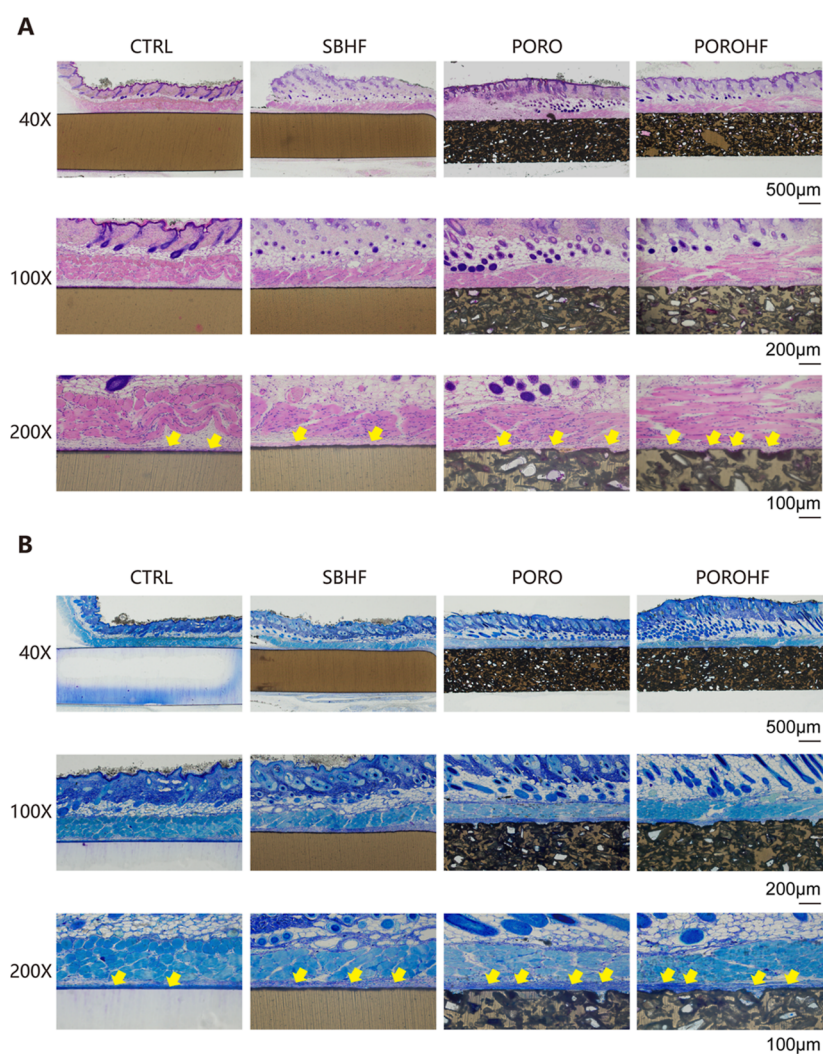


**Figure 4.** Ectopic bone matrix formation on the hard tissue slices of POROHF, PORO, SBHF, and CTRL groups 8 weeks after implantation. (A) HE staining; (B) Toluidine blue staining.

biological effects on MC3T3-E1 cells. Results showed that porous zirconia with 50% porosity and a mean pore size of 167  $\mu\text{m}$  promoted the greatest adhesion, proliferation, and differentiation among all porous groups. Nonetheless, when compared with a control group (polystyrene), porous zirconia exhibited an inhibitory effect on osteogenesis. A similar inhibitory effect of porous zirconia on osteogenesis was also observed in our previous experiments.<sup>20</sup>

The concept of a “micro–nano-porous zirconia structure” was innovatively introduced in our work, i.e., the production of nanoscale granular structures combined with microscale porous structures. The micro-/nano-structured porous group showed superior osteogenic effects to SBHF and PORO; this was supported by a number of osteogenic indicators including the early osteogenic transcription factor RUNX2, the middle-period osteogenesis-related enzyme ALP, and the late period osteogenesis assay ARS. Recent studies have shown that combining nano- and micro-scale surface morphology may exert a physical containment effect of contact guidance on cells, modulating cellular responses, inducing changes in cell adhesion and gene expression, and thus controlling cell fate.<sup>48–52</sup> Elena Sima et al.<sup>7</sup> showed that the microgroove arrays combined with nanoroughened sidewalls on the surface of zirconia specimens treated with a femtosecond laser

facilitated osteogenic differentiation of hMSCs. The micro- or nano-structure may affect cell differentiation through mechanotransduction. The mechanical signals are converted into biochemical signals via biomolecules and/or pathways such as integrins, FAK, MAPK, and Hedgehog, or via direct impact through the cytoskeleton on the nucleus, resulting in cytoskeletal rearrangement and changes in cell morphology and osteogenic gene expression.<sup>53–55</sup>

Angiogenesis of the implant material is fundamental and can determine the amount of new bone formation.<sup>56</sup> Pores encourage vascularization in bone tissue formation.<sup>43</sup> Our results revealed that a porous zirconia surface can enhance expression of *VEGF* and *ANG-1* of hBMSCs, while the micro-/nano-structured porous group achieved the best stimulatory effect. VEGF is a crucial angiogenic factor that has the greatest and most important biological action in neovascularization,<sup>57,58</sup> while *ANG-1* is important in the late stages of blood vessel development, which include endothelial sprout stability and interaction with pericytes.<sup>59</sup> The increased production of VEGF and *ANG-1* might have paracrine effects on host angiogenic cells, thus promoting angiogenesis in vivo.<sup>58</sup>

**Micro-/Nano-structured Porous Zirconia Stimulated Ectopic Bone Formation In Vivo.** Porous implants have been shown to promote osteogenesis in vivo. A preclinical

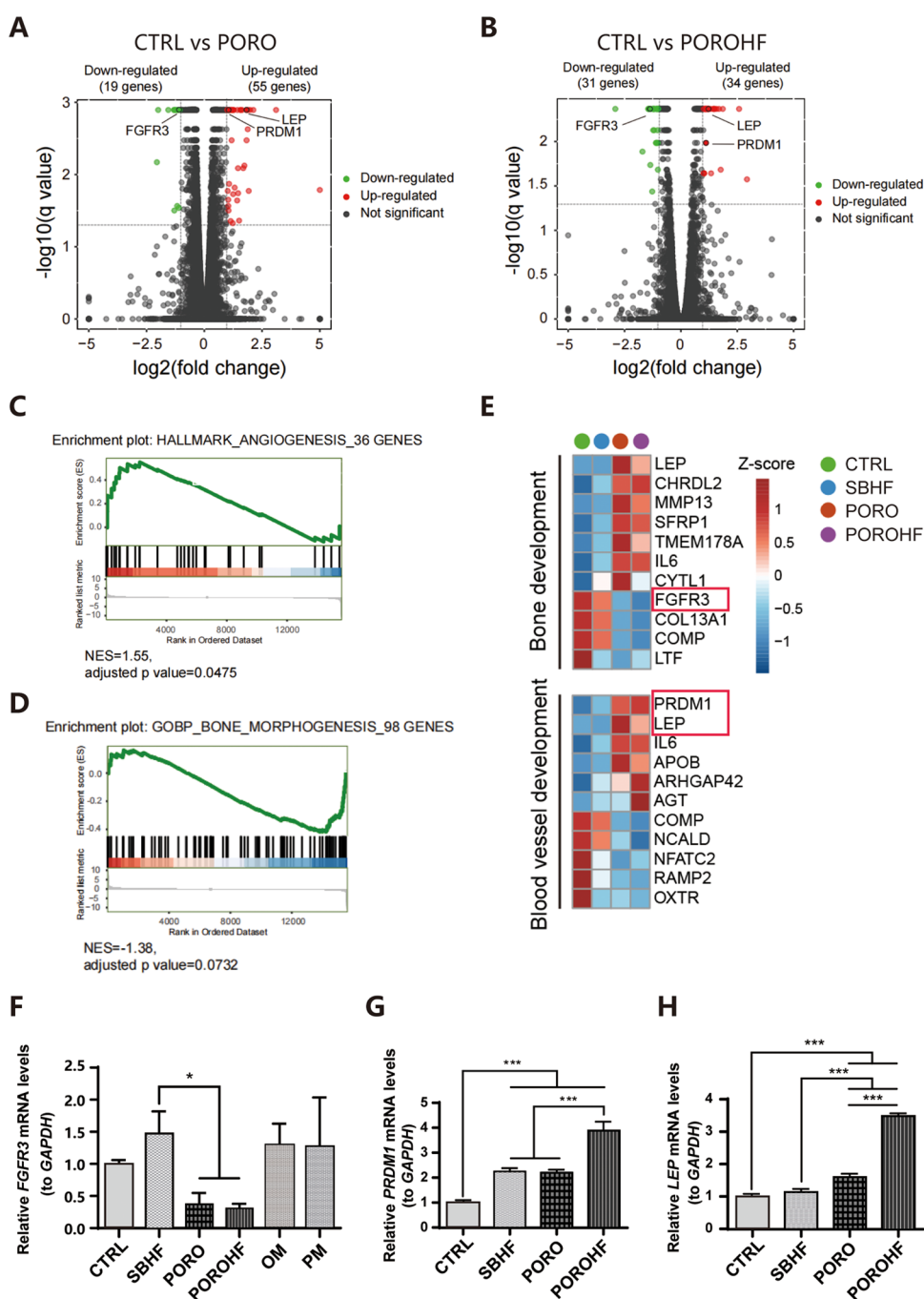


**Figure 5.** Gene expression analysis of hBMSCs on POROHF, PORO, SBHF, and CTRL zirconia specimens. (A,B) Volcano plot of significantly up-regulated (PORO vs CTRL > 2/POROHF vs CTRL > 2,  $Q$  value < 0.05) and down-regulated (CTRL vs PORO > 2/CTRL vs POROHF > 2,  $Q$  value < 0.05) genes. Three genes associated with bone development or blood vessel development are highlighted. Green dots: significantly down-regulated genes. Red dots: significantly up-regulated genes; Gray dots: not significantly up- or down-regulated genes. (C,D) GSEA shows the enrichment of angiogenesis (C) and bone morphogenesis (D) gene sets in the PORO group. (E) Heatmap shows the z-score of gene expression among the 4 samples. Significantly differential expressed genes enriched in the GO term associated with bone development and blood vessel development were displayed. Three critical target genes associated with bone or blood vessel development is framed in red. (F–H) Verification of representative DEGs by RT-qPCR. Data are presented as mean  $\pm$  SD.  $n = 3$ . \* $p < 0.05$ , \*\* $p < 0.01$ , \*\*\* $p < 0.001$ .

meta-analysis of relevant animal studies indicated that porous-surface titanium or tantalum implants promoted bone formation, while their use had no significant effect on bone-implant contact rate (BIC %).<sup>60</sup> Although Sanon et al.<sup>19</sup> fabricated porous zirconia implants with surface pore sizes of 10–50  $\mu\text{m}$ , they only explored the mechanical properties. In vivo studies with porous zirconia implants are still lacking.

Subcutaneous ectopic osteogenesis in nude mice can exclude the recipient's own osteogenic factors; the cellular origin of new bone can be easily explained. In in vitro experiments, seed cells were inoculated on the surface of the material to clarify the promoting effect of POROHF on osteogenic differentiation of hBMSCs. To confirm further the in vitro results, we employed nude mice transplantation to investigate the differentiation potential of the POROHF group in vivo (Figure

S3A). After 8 weeks of implantation, acidophilic tissue under HE staining and blue tissue under toluidine blue staining could be found clinging to the surface of the materials. As shown in Figure 4, POROHF surfaces demonstrated the most significant ectopic bone matrix formation and the thickest neo-bone layer. The PORO group demonstrated a relatively high level of bone matrix formation as well. These findings supported *in vitro* experiments and demonstrated the efficiency of micro-/nano-structured porous zirconia in promoting new bone formation. HE stained sections of the heart, liver, spleen, lung, and kidney showed normal tissue morphology with no obvious inflammatory cell infiltration (Figure S3B).

Within the limitations of our experiments, the potential of porous zirconia in promoting bone formation was confirmed by ectopic bone formation; further, porous surfaces with nano-structures exhibited greater potential. Rezaei et al. created hierarchical roughened groove-like morphology with meso-, micro-, and nano-scale defined structures on zirconia and observed increased capability for osseointegration compared to machined zirconia.<sup>31</sup> Further *in situ* bone generation experiments are needed to verify the osseointegration of micro-/nano-structured porous zirconia implants.

Based on the above *in vitro* and *in vivo* results, the surface modification approach combining nano-scale structures and micro-scale pores proposed in this study shows promise in its ability to enhance osseointegration of zirconia implants, thus reducing the implants' failure rate and expanding their clinical application.

**Gene Expression Profiling by RNA Sequencing.** To gain insight into the potential mechanisms governing the osteogenic process of POROHF and PORO zirconia, gene expression profiles of hBMSCs cultured on the different surfaces were analyzed by RNA sequencing. Differences in gene expression between POROHF and CTRL, and between PORO and CTRL, were analyzed by comparing their expression profiles. For the POROHF versus CTRL comparison, the volcano plot showed 34 genes were significantly upregulated ( $\log_2$  fold change  $> 2$ ,  $Q$  value  $< 0.05$ ) and 31 genes were significantly downregulated ( $\log_2$  fold change  $> 2$ ,  $Q$  value  $< 0.05$ ) in hBMSCs. Three genes associated with bone or blood vessel development are highlighted (Figure 5B). For the PORO versus CTRL comparison, 55 genes were significantly upregulated ( $\log_2$  fold change  $> 2$ ,  $Q$  value  $< 0.05$ ) and 19 genes were significantly downregulated ( $\log_2$  fold change  $> 2$ ,  $Q$  value  $< 0.05$ ) in hBMSCs. Three genes associated with bone or blood vessel development are highlighted (Figure 5A). GO analysis indicated significantly regulated genes (POROHF vs CTRL  $> 2$ /CTRL vs POROHF  $> 2$ /PORO vs CTRL  $> 2$ /CTRL vs PORO  $> 2$ ,  $Q$  value  $< 0.05$ ) were enriched in the term related to bone and blood vessel development (Figure S4A,B). GSEA showed enrichment of angiogenesis (Figure 5C) and bone morphogenesis (Figure 5D) gene sets in the PORO group. GSEA needs to be analyzed with all genes in the bone morphogenesis or angiogenesis gene set. However, in the POROHF group, mainly genes with significant differences were associated with osteogenesis and angiogenesis. Therefore, analyzing all genes yielded no results. A heatmap with the  $z$ -score of gene expression among the four samples is shown. DEGs enriched in the GO term associated with bone development and blood vessel development are shown (Figure 5E). Further, RT-qPCR was performed to confirm the expression levels of representative DEGs. Both the POROHF and PORO group showed significant reductions in

fibroblast growth factor receptor 3 (*FGFR3*) expression ( $p < 0.05$ ) (Figure 5F). *PRDM1* and *LEP* were significantly upregulated in the POROHF group ( $p < 0.001$ ) (Figure 5G,H).

*FGFR3* has been reported to inhibit osteogenesis in endochondral ossification.<sup>61</sup> *In vivo* analysis showed a significant increase in osteoid formation in the long bones of 4 month-old *FGFR3*<sup>-/-</sup> mice; staining of osteogenesis-related markers was also increased.<sup>62</sup> Moreover, BMSCs of *FGFR3* knockout mice expressed more ALP *in vitro*.<sup>62</sup> *FGFR3* is a negative regulator of hedgehog signaling.<sup>63</sup> Several studies have indicated the potential role of the hedgehog pathway in mediating the response of osteoblasts to biomaterial topographies. Lin et al.<sup>55</sup> showed that the micro-/nano-textured surface topography activated hedgehog signaling compared to smooth and micro-structured titanium surfaces. Moreover, stimulation of the hedgehog pathway in MSCs increased the expression of osteogenic genes (e.g., *RUNX2* and *BMPs*).<sup>64</sup> We speculate that micro-/nano-structured porous zirconia inhibits expression of *FGFR3* promotes activation of hedgehog signaling and finally upregulates osteogenic gene expression in hBMSCs.

*PRDM1* (PR/SET domain 1) is a candidate in heart development. Mutation of *PRDM1* in second heart fields leads to arterial pole defects.<sup>65</sup> *LEP*, widely recognized as a proangiogenic chemical, is a physiological regulator of the capillary network in skeletal muscle and stimulates VEGFA production by skeletal myocytes.<sup>66</sup> The high expression of *PRDM1* and *LEP* implied they may play important roles in the stimulation of angiogenesis by micro-/nano-structured porous zirconia. During the osseointegration process of biomaterials, angiogenesis serves as a starting point for progenitor cell migration and is crucial for matrix deposition by supplying nutrients required for bone formation.<sup>53</sup> The promotion of new bone formation *in vivo* by micro-/nano-structured porous surfaces in this study is likely to be related to upregulated expression of angiogenic factors. Altogether, our study detected critical target genes and identified for the first time the molecular mechanisms triggered by micro-/nano-structured porous zirconia on hBMSC osteogenesis and angiogenesis. Further gene overexpression and knockdown experiments are needed to validate the above conjectures.

This study demonstrated the effects of micro-/nano-structured porous zirconia on the adhesion, proliferation, osteogenesis, and angiogenesis of hBMSCs, and the underlying mechanisms were preliminarily explored. Further studies are needed to investigate the *in situ* osteogenesis effect and mechanical strength of micro-/nano-structured porous zirconia. In addition, the particular pathways underlying the effects on osteogenesis and angiogenesis will require further exploration.

## CONCLUSIONS

This study established a micro-/nano-structured porous zirconia surface possessing micro-scale pores and nano-scale secondary structure that can promote osteogenic differentiation and angiogenesis of hBMSCs, as compared with the PORO group, and perform better than SBHF both *in vitro* and *in vivo*. It has no significant impact on the flexural strength of zirconia and can potentially become an effective surface modification modality for improved osseointegration of zirconia implants, which will be crucial for future clinical applications. It is speculated that micro-/nano-structured

porous zirconia surfaces can promote osteogenic differentiation of hBMSCs by inhibiting the FGFR3 expression and promote angiogenesis by upregulating PRDM1 and LEP. Additional experiments are needed to investigate further the underlying mechanisms.

## ■ ASSOCIATED CONTENT

### SI Supporting Information

The Supporting Information is available free of charge at <https://pubs.acs.org/doi/10.1021/acsami.2c22736>.

FESEM observation of hBMSCs morphology on POROHF, PORO, SBHF and CTRL surfaces after 7 d of culture at 100×, 500×, 1000×, and 2000× magnification, osteogenic inducer detection and osteogenic differentiation of hBMSCs in CTRL, SBHF, PORO, POROHF, OM, and PM groups in vitro, ectopic bone formation of POROHF, PORO, SBHF, and CTRL zirconia specimens, and GO analysis (PDF)

## ■ AUTHOR INFORMATION

### Corresponding Authors

**Ping Zhang** – Department of Prosthodontics, Peking University School and Hospital of Stomatology & National Center of Stomatology & National Clinical Research Center for Oral Diseases & National Engineering Laboratory for Digital and Material Technology of Stomatology & Beijing Key Laboratory of Digital Stomatology & Research Center of Engineering and Technology for Computerized Dentistry Ministry of Health & NMPA Key Laboratory for Dental Materials, Beijing 100081, PR China; Email: [zhangping332@bjmu.edu.cn](mailto:zhangping332@bjmu.edu.cn)

**Lei Zhang** – Department of Prosthodontics, Peking University School and Hospital of Stomatology & National Center of Stomatology & National Clinical Research Center for Oral Diseases & National Engineering Laboratory for Digital and Material Technology of Stomatology & Beijing Key Laboratory of Digital Stomatology & Research Center of Engineering and Technology for Computerized Dentistry Ministry of Health & NMPA Key Laboratory for Dental Materials, Beijing 100081, PR China; Email: [drzhanglei@yeah.net](mailto:drzhanglei@yeah.net)

### Authors

**Yuan Gao** – Department of Prosthodontics, Peking University School and Hospital of Stomatology & National Center of Stomatology & National Clinical Research Center for Oral Diseases & National Engineering Laboratory for Digital and Material Technology of Stomatology & Beijing Key Laboratory of Digital Stomatology & Research Center of Engineering and Technology for Computerized Dentistry Ministry of Health & NMPA Key Laboratory for Dental Materials, Beijing 100081, PR China; [orcid.org/0000-0002-6793-9149](https://orcid.org/0000-0002-6793-9149)

**Qian Ding** – Department of Prosthodontics, Peking University School and Hospital of Stomatology & National Center of Stomatology & National Clinical Research Center for Oral Diseases & National Engineering Laboratory for Digital and Material Technology of Stomatology & Beijing Key Laboratory of Digital Stomatology & Research Center of Engineering and Technology for Computerized Dentistry Ministry of Health & NMPA Key Laboratory for Dental Materials, Beijing 100081, PR China

**Wenjin Li** – Department of Prosthodontics, Peking University School and Hospital of Stomatology & National Center of Stomatology & National Clinical Research Center for Oral Diseases & National Engineering Laboratory for Digital and Material Technology of Stomatology & Beijing Key Laboratory of Digital Stomatology & Research Center of Engineering and Technology for Computerized Dentistry Ministry of Health & NMPA Key Laboratory for Dental Materials, Beijing 100081, PR China

**Ranli Gu** – Department of Prosthodontics, Peking University School and Hospital of Stomatology & National Center of Stomatology & National Clinical Research Center for Oral Diseases & National Engineering Laboratory for Digital and Material Technology of Stomatology & Beijing Key Laboratory of Digital Stomatology & Research Center of Engineering and Technology for Computerized Dentistry Ministry of Health & NMPA Key Laboratory for Dental Materials, Beijing 100081, PR China

Complete contact information is available at:

<https://pubs.acs.org/doi/10.1021/acsami.2c22736>

### Author Contributions

Y.G.: design; data acquisition; formal analysis and interpretation; writing: original draft; and final approval. Q.D.: design; formal analysis and interpretation; writing: review and revising; and final approval. Y.G. and Q.D. contributed equally to this paper. W.L.: data acquisition; writing: review and revising; and final approval. R.G.: data acquisition; writing: review and revising; and final approval. P.Z.: conceptualization; design; writing: review and revising; and final approval. L.Z.: conceptualization; funding acquisition; design; writing: review and revising; and final approval.

### Funding

This work was supported by Capital Health Research and Development of Special Fund (grant number: 2020-2-4104) and Guangdong Basic and Applied Basic Research Foundation (2019A1515110889).

### Notes

The authors declare no competing financial interest.

## ■ ACKNOWLEDGMENTS

We thank Xinjie Liang (Zhong Xin Tang Guo Ye Medical Technology Co., Ltd., China) for providing the porous zirconia materials, and Dr. Hao Liu for the experiment platform and useful advice.

## ■ ABBREVIATIONS

hBMSCs, human bone marrow mesenchymal stem cells  
VEGFB, vascular endothelial growth factor B  
ANGPT1, angiopoietin 1  
3Y-TZP, 3 mol % yttrium oxide stabilized polycrystalline tetragonal phase zirconia  
3D, three-dimensional  
LEP, LEPTIN  
CTRL, control group  
SBHF, sandblasting and hydrofluoric acid etching group  
PORO, porous group  
PMMA, polymethyl methacrylate  
POROHF, porous plus hydrofluoric acid group  
dH<sub>2</sub>O, deionized water  
FESEM, field emission scanning electron microscopy  
EDS, energy dispersive spectrometer

FBS, fetal bovine serum  
 $\alpha$ -MEM,  $\alpha$ -minimum essential medium  
 Pen/Strep, penicillin/streptomycin  
 PM, proliferation medium  
 OM, osteogenic medium  
 PBS, phosphate-buffered saline  
 LSCM, laser scanning confocal microscopy  
 CCK8, cell counting kit-8  
 BSA, bovine serum albumin  
 ALP, alkaline phosphatase  
 BCA, bicinchoninic acid  
 ARS, alizarin red S  
 RT-qPCR, real-time quantitative PCR  
 ANG-1, ANGPT1  
 HE, hematoxylin and eosin  
 FPKM, fragments per kilobase of exon model per million mapped fragments  
 DEGs, differentially expressed genes  
 GO, gene ontology  
 GSEA, gene set enrichment analysis  
 BIC, bone-implant contact  
 FGFR3, fibroblast growth factor receptor 3  
 PRDM1, PR/SET domain 1

## REFERENCES

- Schünemann, F. H.; Galárraga-Vinueza, M. E.; Magini, R.; Fredel, M.; Silva, F.; Souza, J. C. M.; Zhang, Y.; Henriques, B. Zirconia surface modifications for implant dentistry. *Mater. Sci. Eng., C* **2019**, *98*, 1294–1305.
- Roehling, S.; Astasov-Frauenhoffer, M.; Hauser-Gerspach, I.; Braissant, O.; Woelfler, H.; Waltimo, T.; Kniha, H.; Gahlert, M. In Vitro Biofilm Formation on Titanium and Zirconia Implant Surfaces. *J. Periodontol.* **2017**, *88*, 298–307.
- Haro Adánez, M.; Nishihara, H.; Att, W. A systematic review and meta-analysis on the clinical outcome of zirconia implant-restoration complex. *J. Prosthodont. Res.* **2018**, *62*, 397–406.
- Roehling, S.; Schlegel, K. A.; Woelfler, H.; Gahlert, M. Zirconia compared to titanium dental implants in preclinical studies-A systematic review and meta-analysis. *Clin. Oral Implants Res.* **2019**, *30*, 365–395.
- Flamant, Q.; García Marro, F.; Roa Rovira, J. J.; Anglada, M. Hydrofluoric acid etching of dental zirconia. Part 1: etching mechanism and surface characterization. *J. Eur. Ceram. Soc.* **2016**, *36*, 121–134.
- Bacchelli, B.; Giavaresi, G.; Franchi, M.; Martini, D.; De Pasquale, V.; Trirè, A.; Fini, M.; Giardino, R.; Ruggeri, A. Influence of a zirconia sandblasting treated surface on peri-implant bone healing: An experimental study in sheep. *Acta Biomater.* **2009**, *5*, 2246–2257.
- Elena Sima, L.; Bonciu, A.; Baci, M.; Anghel, I.; Dumitrescu, L. N.; Rusen, L.; Dinca, V. Bioinstructive Micro-Nanotextured Zirconia Ceramic Interfaces for Guiding and Stimulating an Osteogenic Response In Vitro. *Nanomaterials* **2020**, *10*, 2465.
- Henningsen, A.; Smeets, R.; Heuberger, R.; Jung, O. T.; Hanken, H.; Heiland, M.; Cacaci, C.; Precht, C. Changes in surface characteristics of titanium and zirconia after surface treatment with ultraviolet light or non-thermal plasma. *Eur. J. Oral Sci.* **2018**, *126*, 126–134.
- Pardun, K.; Treccani, L.; Volkmann, E.; Streckbein, P.; Heiss, C.; Gerlach, J. W.; Maendl, S.; Rezwan, K. Magnesium-containing mixed coatings on zirconia for dental implants: mechanical characterization and in vitro behavior. *J. Biomater. Appl.* **2015**, *30*, 104–118.
- Li, H.; Xie, Y.; Li, K.; Huang, L.; Huang, S.; Zhao, B.; Zheng, X. Microstructure and wear behavior of graphene nanosheets-reinforced zirconia coating. *Ceram. Int.* **2014**, *40*, 12821–12829.
- Oh, G.-J.; Yoon, J.-H.; Vu, V. T.; Ji, M.-K.; Kim, J.-H.; Kim, J.-W.; Yim, E.-K.; Bae, J.-C.; Park, C.; Yun, K.-D.; Lim, H.-P.; Park, S.-W.; Fisher, J. G. Surface Characteristics of Bioactive Glass-Infiltrated Zirconia with Different Hydrofluoric Acid Etching Conditions. *J. Nanosci. Nanotechnol.* **2017**, *17*, 2645–2648.
- Saulacic, N.; Erdösi, R.; Bosshardt, D. D.; Gruber, R.; Buser, D. Acid and alkaline etching of sandblasted zirconia implants: a histomorphometric study in miniature pigs. *Clin. Implant Dent. Relat. Res.* **2014**, *16*, 313–322.
- Ding, Q.; Zhang, R.; Zhang, L.; Sun, Y.; Xie, Q. Effects of Different Microstructured Surfaces on the Osseointegration of CAD/CAM Zirconia Dental Implants: An Experimental Study in Rabbits. *Int. J. Oral Maxillofac. Implants* **2020**, *35*, 1113–1121.
- Asgharzadeh Shirazi, H.; Ayatollahi, M. R.; Asnafi, A. To reduce the maximum stress and the stress shielding effect around a dental implant-bone interface using radial functionally graded biomaterials. *Comput. Methods Biomech. Biomed. Eng.* **2017**, *20*, 750–759.
- Wei, T.; Zhang, X. W.; Sun, H. Q.; Mao, M. Y. [Selective laser sintering and performances of porous titanium implants]. *Huaxi Kouqiang Yixue Zazhi* **2018**, *36*, 532–538.
- Kumar, P.; Kumar, V.; Kumar, R.; Kumar, R.; Pruncu, C. I. Fabrication and characterization of ZrO<sub>2</sub> incorporated SiO<sub>2</sub>-CaO-P<sub>2</sub>O<sub>5</sub> bioactive glass scaffolds. *J. Mech. Behav. Biomed. Mater.* **2020**, *109*, 103854.
- Dantas, T. A.; Roedel, S.; Mesquita-Guimarães, J.; Pinto, P.; Souza, J. C. M.; Fredel, M. C.; Silva, F. S.; Henriques, B. Sliding behavior of zirconia porous implant surfaces against bone. *J. Biomed. Mater. Res., Part B* **2019**, *107*, 1113–1121.
- Sakthiabirami, K.; Kang, J. H.; Jang, J. G.; Soundharajan, V.; Lim, H. P.; Yun, K. D.; Park, C.; Lee, B. N.; Yang, Y. P.; Park, S. W. Hybrid porous zirconia scaffolds fabricated using additive manufacturing for bone tissue engineering applications. *Mater. Sci. Eng., C* **2021**, *123*, 111950.
- Sanon, C.; Chevalier, J.; Douillard, T.; Cattani-Lorente, M.; Scherrer, S. S.; Gremillard, L. A new testing protocol for zirconia dental implants. *Dent. Mater.* **2015**, *31*, 15–25.
- Wang, Z.; Ding, Q.; Gao, Y.; Ma, Q. Q.; Zhang, L.; Ge, X. Y.; Sun, Y. C.; Xie, Q. F. Effect of porous zirconia ceramics on proliferation and differentiation of osteoblasts. *Beijing Daxue Xuebao, Yixueban* **2022**, *54*, 31–39.
- Garvie, R. C.; Nicholson, P. S. Phase Analysis in Zirconia Systems. *J. Am. Ceram. Soc.* **1972**, *55*, 303–305.
- Toraya, H.; Yoshimura, M.; Somiya, S. Calibration Curve for Quantitative-Analysis of the Monoclinic-Tetragonal ZrO<sub>2</sub> System by X-Ray-Diffraction. *J. Am. Ceram. Soc.* **1984**, *67*, C119–C121.
- Kim, D.; Perte, G.; Trapnell, C.; Pimentel, H.; Kelley, R.; Salzberg, S. L. TopHat2: accurate alignment of transcriptomes in the presence of insertions, deletions and gene fusions. *Genome Biol.* **2013**, *14*, R36.
- Trapnell, C.; Roberts, A.; Goff, L.; Perte, G.; Kim, D.; Kelley, D. R.; Pimentel, H.; Salzberg, S. L.; Rinn, J. L.; Pachter, L. Differential gene and transcript expression analysis of RNA-seq experiments with TopHat and Cufflinks. *Nat. Protoc.* **2012**, *7*, 562–578.
- Hotchkiss, K. M.; Reddy, G. B.; Hyzy, S. L.; Schwartz, Z.; Boyan, B. D.; Olivares-Navarrete, R. Titanium surface characteristics, including topography and wettability, alter macrophage activation. *Acta Biomater.* **2016**, *31*, 425–434.
- Bergemann, C.; Duske, K.; Nebe, J. B.; Schöne, A.; Bulnheim, U.; Seitz, H.; Fischer, J. Microstructured zirconia surfaces modulate osteogenic marker genes in human primary osteoblasts. *J. Mater. Sci.: Mater. Med.* **2015**, *26*, 5350.
- Hao, L.; Lawrence, J.; Chian, K. S. Osteoblast cell adhesion on a laser modified zirconia based bioceramic. *J. Mater. Sci.: Mater. Med.* **2005**, *16*, 719–726.
- Xu, X.; Cheng, L.; Zhao, X.; Wang, J.; Chen, X. Micro-/nano-Periodic Surface Structures and Performance of Stainless Steel Machined Using Femtosecond Lasers. *Micromachines* **2022**, *13*, 976.
- Yigit, O.; Dikici, B.; Ozdemir, N. Hydrothermal synthesis of nanocrystalline hydroxyapatite-graphene nanosheet on Ti-6Al-7Nb: mechanical and in vitro corrosion performance. *J. Mater. Sci.: Mater. Med.* **2021**, *32*, 40.

- (30) Wang, T.; Wan, Y.; Liu, Z. Effects of Superimposed Micro/Nano-Structured Titanium Alloy Surface on Cellular Behaviors In Vitro. *Adv. Eng. Mater.* **2016**, *18*, 1259–1266.
- (31) Rezaei, N. M.; Hasegawa, M.; Ishijima, M.; Nakhaei, K.; Okubo, T.; Taniyama, T.; Ghassemi, A.; Tahsili, T.; Park, W.; Hirota, M.; Ogawa, T. Biological and osseointegration capabilities of hierarchically (meso-/micro-/nano-scale) roughened zirconia. *Int. J. Nanomed.* **2018**, *13*, 3381–3395.
- (32) Ding, Q.; Zhang, L.; Bao, R.; Zheng, G.; Sun, Y. C.; Xie, Q. F. Effects of different surface treatments on the cyclic fatigue strength of one-piece CAD/CAM zirconia implants. *J. Mech. Behav. Biomed.* **2018**, *84*, 249–257.
- (33) Hadjicharalambous, C.; Buyakov, A.; Buyakova, S.; Kulkov, S.; Chatzinikolaïdou, M. Porous alumina, zirconia and alumina/zirconia for bone repair: fabrication, mechanical and in vitro biological response. *Biomed. Mater.* **2015**, *10*, 025012.
- (34) Denry, I. How and when does fabrication damage adversely affect the clinical performance of ceramic restorations? *Dent. Mater.* **2013**, *29*, 85–96.
- (35) Scherrer, S. S.; Lohbauer, U.; Della Bona, A.; Vichi, A.; Tholey, M. J.; Kelly, J. R.; van Noort, R.; Cesar, P. F. ADM guidance-Ceramics: guidance to the use of fractography in failure analysis of brittle materials. *Dent. Mater.* **2017**, *33*, 599–620.
- (36) Ma, Q.; Ding, Q.; Zhang, L.; Sun, Y.; Xie, Q. Surface Characteristics and Flexural Strength of Porous-Surface Designed Zirconia Manufactured via Stereolithography. *J. Prosthodontics* **2022**, *1* Epub ahead of print.
- (37) Wang, K.; Geng, J.; Jones, D.; Xu, W. Comparison of the fracture resistance of dental implants with different abutment taper angles. *Mater. Sci. Eng., C* **2016**, *63*, 164–171.
- (38) Anselme, K. Osteoblast adhesion on biomaterials. *Biomaterials* **2000**, *21*, 667–681.
- (39) Lv, L.; Liu, Y.; Zhang, P.; Zhang, X.; Liu, J.; Chen, T.; Su, P.; Li, H.; Zhou, Y. The nanoscale geometry of TiO<sub>2</sub> nanotubes influences the osteogenic differentiation of human adipose-derived stem cells by modulating H3K4 trimethylation. *Biomaterials* **2015**, *39*, 193–205.
- (40) Velnar, T.; Bunc, G.; Klobucar, R.; Gradisnik, L. Biomaterials and host versus graft response: a short review. *Bosnian J. Basic Med. Sci.* **2016**, *16*, 82–90.
- (41) Zemtsova, E. G.; Yudintceva, N. M.; Morozov, P. E.; Valiev, R. Z.; Smirnov, V. M.; Shevtsov, M. A. Improved osseointegration properties of hierarchical microtopographic/nanotopographic coatings fabricated on titanium implants. *Int. J. Nanomed.* **2018**, *13*, 2175–2188.
- (42) Liu, Y.; Rath, B.; Tingart, M.; Eschweiler, J. Role of implants surface modification in osseointegration: A systematic review. *J. Biomed. Mater. Res., Part A* **2020**, *108*, 470–484.
- (43) Karageorgiou, V.; Kaplan, D. Porosity of 3D biomaterial scaffolds and osteogenesis. *Biomaterials* **2005**, *26*, 5474–5491.
- (44) Cheng, A.; Humayun, A.; Cohen, D. J.; Boyan, B. D.; Schwartz, Z. Additively manufactured 3D porous Ti-6Al-4V constructs mimic trabecular bone structure and regulate osteoblast proliferation, differentiation and local factor production in a porosity and surface roughness dependent manner. *Biofabrication* **2014**, *6*, 045007.
- (45) Natsuki, B.; Takemoto, M.; Fujibayashi, S.; Neo, M.; Kokubo, T.; Nakamura, T. Pore throat size and connectivity determine bone and tissue ingrowth into porous implants: three-dimensional micro-CT based structural analyses of porous bioactive titanium implants. *Biomaterials* **2006**, *27*, 5892–5900.
- (46) Fu, Q.; Rahaman, M. N.; Bal, B. S.; Brown, R. F. Proliferation and function of MC3T3-E1 cells on freeze-cast hydroxyapatite scaffolds with oriented pore architectures. *J. Mater. Sci.: Mater. Med.* **2009**, *20*, 1159–1165.
- (47) Chang, B. S.; Lee, C. K.; Hong, K. S.; Youn, H. J.; Ryu, H. S.; Chung, S. S.; Park, K. W. Osteoconduction at porous hydroxyapatite with various pore configurations. *Biomaterials* **2000**, *21*, 1291–1298.
- (48) Costa, P.; Almeida, F. V.; Connelly, J. T. Biophysical signals controlling cell fate decisions: how do stem cells really feel? *Int. J. Biochem. Cell Biol.* **2012**, *44*, 2233–2237.
- (49) Hao, J.; Zhang, Y.; Jing, D.; Shen, Y.; Tang, G.; Huang, S.; Zhao, Z. Mechanobiology of mesenchymal stem cells: Perspective into mechanical induction of MSC fate. *Acta Biomater.* **2015**, *20*, 1–9.
- (50) Hiew, V. V.; Simat, S. F. B.; Teoh, P. L. The Advancement of Biomaterials in Regulating Stem Cell Fate. *Stem Cell Rev. Rep.* **2018**, *14*, 43–57.
- (51) Krishna, L.; Dhamodaran, K.; Jayadev, C.; Chatterjee, K.; Shetty, R.; Khora, S. S.; Das, D. Nanostructured scaffold as a determinant of stem cell fate. *Stem Cell Res. Ther.* **2016**, *7*, 188.
- (52) MacQueen, L.; Sun, Y.; Simmons, C. A. Mesenchymal stem cell mechanobiology and emerging experimental platforms. *J. R. Soc., Interface* **2013**, *10*, 20130179.
- (53) Raines, A. L.; Berger, M. B.; Schwartz, Z.; Boyan, B. D. Osteoblasts grown on microroughened titanium surfaces regulate angiogenic growth factor production through specific integrin receptors. *Acta Biomater.* **2019**, *97*, 578–586.
- (54) da Costa Fernandes, C. J.; Ferreira, M. R.; Bezerra, F. J. B.; Zambuzzi, W. F. Zirconia stimulates ECM-remodeling as a prerequisite to pre-osteoblast adhesion/proliferation by possible interference with cellular anchorage. *J. Mater. Sci.: Mater. Med.* **2018**, *29*, 41.
- (55) Lin, Y.; Huang, Y.; He, J.; Chen, F.; He, Y.; Zhang, W. Role of Hedgehog–Gli1 signaling in the enhanced proliferation and differentiation of MG63 cells enabled by hierarchical micro-/nanotextured topography. *Int. J. Nanomed.* **2017**, *12*, 3267–3280.
- (56) Xia, L.; Ma, W.; Zhou, Y.; Gui, Z.; Yao, A.; Wang, D.; Takemura, A.; Uemura, M.; Lin, K.; Xu, Y. Stimulatory Effects of Boron Containing Bioactive Glass on Osteogenesis and Angiogenesis of Polycaprolactone: In Vitro Study. *BioMed Res. Int.* **2019**, *2019*, 1–12.
- (57) Ruskowska-Ciastek, B.; Sokup, A.; Socha, M. W.; Ruprecht, Z.; Hałas, L.; GÓralczyk, B.; GÓralczyk, K.; Gadomska, G.; Rośc, D. A preliminary evaluation of VEGF-A, VEGFR1 and VEGFR2 in patients with well-controlled type 2 diabetes mellitus. *J. Zhejiang Univ., Sci., B* **2014**, *15*, 575–581.
- (58) Zhang, Z.; Neiva, K. G.; Lingen, M. W.; Ellis, L. M.; Nör, J. E. VEGF-dependent tumor angiogenesis requires inverse and reciprocal regulation of VEGFR1 and VEGFR2. *Cell Death Differ.* **2010**, *17*, 499–512.
- (59) Fukuhara, S.; Sako, K.; Noda, K.; Zhang, J.; Minami, M.; Mochizuki, N. Angiopoietin-1/Tie2 receptor signaling in vascular quiescence and angiogenesis. *Histol. Histopathol.* **2010**, *25*, 387–396.
- (60) Ahmed, A.; Al-Rasheed, A.; Badwelan, M.; Alghamdi, H. S. Peri-Implant bone response around porous-surface dental implants: A preclinical meta-analysis. *Saudi Dent J.* **2021**, *33*, 239–247.
- (61) Deng, C.; Wynshaw-Boris, A.; Zhou, F.; Kuo, A.; Leder, P. Fibroblast growth factor receptor 3 is a negative regulator of bone growth. *Cell* **1996**, *84*, 911–921.
- (62) Valverde-Franco, G.; Liu, H.; Davidson, D.; Chai, S.; Valderrama-Carvajal, H.; Goltzman, D.; Ornitz, D. M.; Henderson, J. E. Defective bone mineralization and osteopenia in young adult FGFR3<sup>-/-</sup> mice. *Hum. Mol. Genet.* **2004**, *13*, 271–284.
- (63) Naski, M. C.; Colvin, J. S.; Coffin, J. D.; Ornitz, D. M. Repression of hedgehog signaling and BMP4 expression in growth plate cartilage by fibroblast growth factor receptor 3. *Development* **1998**, *125*, 4977–4988.
- (64) Oliveira, F. S.; Bellesini, L. S.; Defino, H. L.; da Silva Herrero, C. F.; Beloti, M. M.; Rosa, A. L. Hedgehog signaling and osteoblast gene expression are regulated by purmorphamine in human mesenchymal stem cells. *J. Cell. Biochem.* **2012**, *113*, 204–208.
- (65) Vincent, S. D.; Mayeuf-Louchart, A.; Watanabe, Y.; Brzezinski, J. A. t.; Miyagawa-Tomita, S.; Kelly, R. G.; Buckingham, M. Prdm1 functions in the mesoderm of the second heart field, where it interacts genetically with Tbx1, during outflow tract morphogenesis in the mouse embryo. *Hum. Mol. Genet.* **2014**, *23*, 5087–5101.
- (66) Nwadozi, E.; Ng, A.; Strömberg, A.; Liu, H. Y.; Olsson, K.; Gustafsson, T.; Haas, T. L. Leptin is a physiological regulator of skeletal muscle angiogenesis and is locally produced by PDGFR $\alpha$  and

PDGFR $\beta$  expressing perivascular cells. *Angiogenesis* **2019**, *22*, 103–115.

## Recommended by ACS

---

### **Chemical Modification of Human Decellularized Extracellular Matrix for Incorporation into Phototunable Hybrid-Hydrogel Models of Tissue Fibrosis**

Rukshika S. Hewawasam, Chelsea M. Magin, *et al.*

MARCH 14, 2023

ACS APPLIED MATERIALS & INTERFACES

READ 

### **In Silico Analysis Reveals the Inhibitory Potential of Madecassic Acid against Entry Factors of SARS-CoV-2**

Abhratanu Ganguly, Prem Rajak, *et al.*

JANUARY 06, 2023

ACS APPLIED BIO MATERIALS

READ 

### **Fibronectin-Enriched Interface Using a Spheroid-Converged Cell Sheet for Effective Wound Healing**

Sung-Won Kim, Suk Ho Bhang, *et al.*

FEBRUARY 22, 2023

ACS APPLIED MATERIALS & INTERFACES

READ 

### **Evaluation of Cellulose–MXene Composite Hydrogel Based Bio-Resistive Random Access Memory Material as Mimics for Biological Synapses**

Trishala R. Desai, Chitra Gurnani, *et al.*

MARCH 28, 2023

ACS APPLIED BIO MATERIALS

READ 

**Get More Suggestions >**

---